

# Spatiotemporal dynamics of future hydrology in the Pearl River Basin: Controls of climate change and land surface

Ying Zhang, Jianping Gan <sup>\*</sup>

Department of Ocean Science, Department of Mathematics and Center for Ocean Research in Hong Kong and Macau, Hong Kong University of Science and Technology, Hong Kong, China

## ARTICLE INFO

### Keywords:

Hydroclimate  
Land surface processes  
Monsoon climate  
Streamflow

## ABSTRACT

*Study region:* The Pearl River Basin in China.

*Study focus:* The hydrological cycle is anticipated to undergo systematic alterations due to climate change, impacting future water resources and ecosystem functions. Driven by an optimized subset of General Circulation Models through a comprehensive framework of multi-level calibrations, we employed a well-validated Soil and Water Assessment Tool to predict streamflow and investigate the underlying dynamics in the basin.

*New hydrological insights for the region:* The combined effects of the variability in regional monsoon climate and land surface processes jointly control the spatiotemporally varied streamflow. There is a highly nonlinear temporal trend, with slight near-term reduction and a significant long-term increase. It is also spatially heterogeneous, with more significant increases in the eastern basin than in the western, attributed to an asymmetrically strengthened/weakened East/South Asian Summer Monsoons. Land use affects the response of streamflow to climate change. Lateral flow is most variable in forested hills due to their high water interception rates, while aquifer flow varies most in agricultural areas with their coarse soils and high water storage capacity; both show an increasing trend during the wet season because of elevated precipitation and a decreasing trend due to increased evapotranspiration during the dry season. Surface flow consistently increases the most in urban regions due to low evaporation and intensified precipitation.

## 1. Introduction

Terrestrial hydrology is a critical component of Earth's system, serving as a vital link between the atmosphere, land, and oceans, and directly influencing water resources and sustaining ecosystem functions (Gleeson et al., 2020). However, hydrological processes have been systematically altered due to climate change, which modifies the water and energy inputs into the hydrological cycle (IPCC, 2021). The land surface modulates the response of water fluxes to climate change by controlling their redistribution and movement in soil profiles (Vereecken et al., 2022). The intricate interactions between land and atmosphere complicate the identification of controlling mechanisms for future hydrological dynamics, thereby hindering the strategy development for water resources (Zhu et al., 2021).

The future evolution of streamflow exhibits varied spatial and temporal patterns, driven by changes in atmospheric and surface radiation budgets under climate change (Zhou et al., 2023). For instance, the Mediterranean shows a significant drying trend at the

<sup>\*</sup> Corresponding author.

E-mail address: [magan@ust.hk](mailto:magan@ust.hk) (J. Gan).

annual scale due to heightened evapotranspiration (ET), while the North Asia is expected to be wetter due to enhanced convective precipitation or snowmelt (Han et al., 2024). In contrast, subtropical areas usually present a mixture of change signals and varying intensity with large uncertainties (Gudmundsson et al., 2019). Moreover, these trends may be nonlinear over time due to complex feedbacks among the components of Earth system (Steffen, 2022). The seasonality of streamflow may shift under uneven precipitation and ET changes (Dai, 2021). For example, in China, winter warming is occurring at four times the rate of summer warming, leading to more intensified decreases in winter flows (Piao et al., 2010). The complex nature of these changes underscores the necessity of conducting regional investigations to capture the streamflow dynamics.

The flow components, composed of surface flow and baseflow, synchronously undergo variations under climate change but receive less attention compared to total flow. These flows respond differently to changes in climate factors. Surface flow heavily depends on precipitation, and its increase may pose a significant risk of pluvial flooding, especially in impervious lands (Wasko et al., 2021). Baseflow, which includes both lateral and aquifer flows, can be positively or negatively correlated with temperature, depending on factors such as snowmelt or increased ET (J. Zhang et al., 2022). Terrain also influences baseflow's response to climate forcing. For example, headwater regions with shallow, surface-connected groundwater are more susceptible to increased ET and precipitation recharge (Miller et al., 2021). The diverse mechanisms of these flow components necessitate process-based hydrological models to simulate the movement of water fluxes within the soil profile (Nandi and Manne, 2020).

Climate factors are the primary drivers of changes in water fluxes, with each factor contributing variably. Precipitation, the main water source, has altered streamflow in most rivers worldwide (Tang and Wang, 2021). In mountainous areas where glacier are significant sources of streamflow, the importance of temperature increases under global warming (Fan et al., 2021). Besides affecting water sources, climate factors also influence streamflow through ET. During cold seasons, ET is primarily limited by energy supply, making solar radiation the most important factor. In contrast, temperature and humidity have a more significant impact on ET during spring and summer (Ahmadi et al., 2022). Besides, slower wind speeds and higher air humidity may partially offset the increased ET demand caused by warming, thereby enhancing runoff (Duan et al., 2017). While the importance of these factors is widely recognized, their bidirectional and diverse effects make it difficult to pinpoint the primary drivers governing the local water budget (Liu et al., 2024; Valipour et al., 2020; S. Wang et al., 2020).

Land use is one of the most important components of the terrestrial system that modulates the response of water fluxes to climate

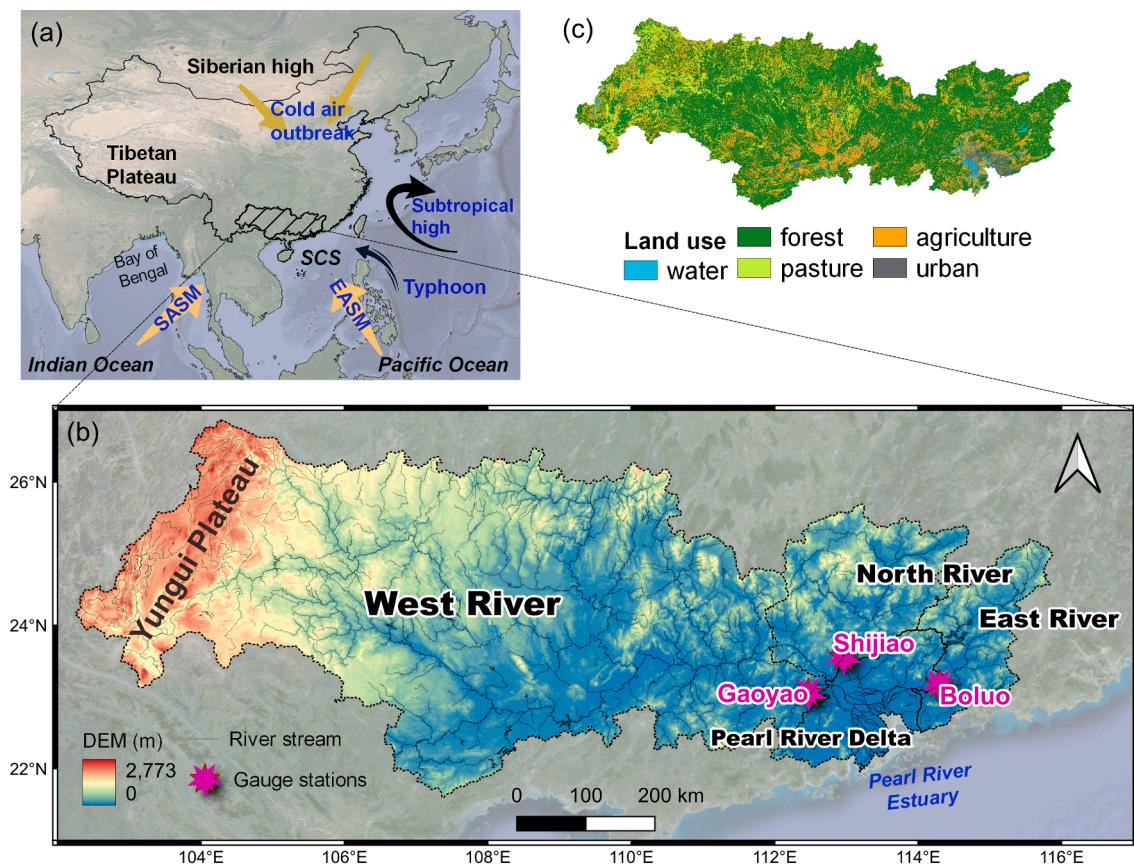


Fig. 1. (a) Location of the Pearl River Basin and monsoon systems, (b) topography, river streams, and control gauge stations, and (c) land use map. EASM and SASM represent the East Asian Summer Monsoon and South Asian Summer Monsoon, respectively. SCS refers to the South China Sea.

change (Yang et al., 2020). It affects runoff primarily through transpiration; plants with a larger leaf area consume more water than others, potentially exacerbating drought conditions. Conversely, urban areas with impervious surfaces cannot store soil water and significantly reduce ET (Zhang et al., 2001). Land use influences the temporal pattern of streamflow by regulating water redistribution within the soil profile. For example, agricultural cultivation and urbanization can exacerbate flooding due to the high ratio of surface flow, whereas reforestation can mitigate the impacts of precipitation extremes on streamflow through higher interception and infiltration rates (Zhang et al., 2020). However, the effects of land use, often intertwined with climate trends, make it difficult to disentangle their contributions to the hydrological dynamics in heterogeneous landscapes (S. Wang et al., 2020).

A reliable climate forcing is a prerequisite for predicting highly variable streamflow (Freedman et al., 2014; Holmes et al., 2020). Global Climate Models (GCMs), especially those recently released in the Coupled Model Intercomparison Project Phase 6 (CMIP6), are powerful tools that integrate atmospheric, oceanic, and terrestrial hydrology processes within Earth systems, providing plausible patterns of global climate change (Brands, 2022; Cannon, 2020). However, when applied at regional scales, these models inevitably introduce biases due to inherent uncertainties, resulting in contradictory predictions (Cook et al., 2020; Winter et al., 2015).

To minimize uncertainties in GCMs, several procedures have been developed for hydrological projection, including GCM evaluation, ensemble construction, and bias correction (Li et al., 2017; Wu and Huang, 2016; Zhu et al., 2021). GCM evaluation assesses each model’s ability to reproduce one or more facets of observations, while bias correction aims to systematically reduce biases in GCM ensembles relative to those observations (Das et al., 2018; Fu et al., 2013). Although there are various methods to evaluate GCMs or correct biases, previous research has primarily focused on climate variables like precipitation and temperature, often neglecting the combined impacts on hydrograph reproduction (Hou et al., 2023). Ensemble construction involves averaging several top-performing GCMs based on their rankings (Lutz et al., 2016; Winter et al., 2015). However, the selection criteria for these GCMs are often unclear, leading to the arbitrary use of models and hindering regional intercomparisons.

We employed a well-validated Soil and Water Assessment Tool (SWAT) for simulating and projecting water fluxes in the Pearl River Basin (PRB). The specific objectives of our research are: 1) to develop a multi-level calibrated framework to construct a GCM subset that reduces hydrological uncertainty, 2) to predict the spatiotemporal distribution of future water fluxes, and 3) to reveal the

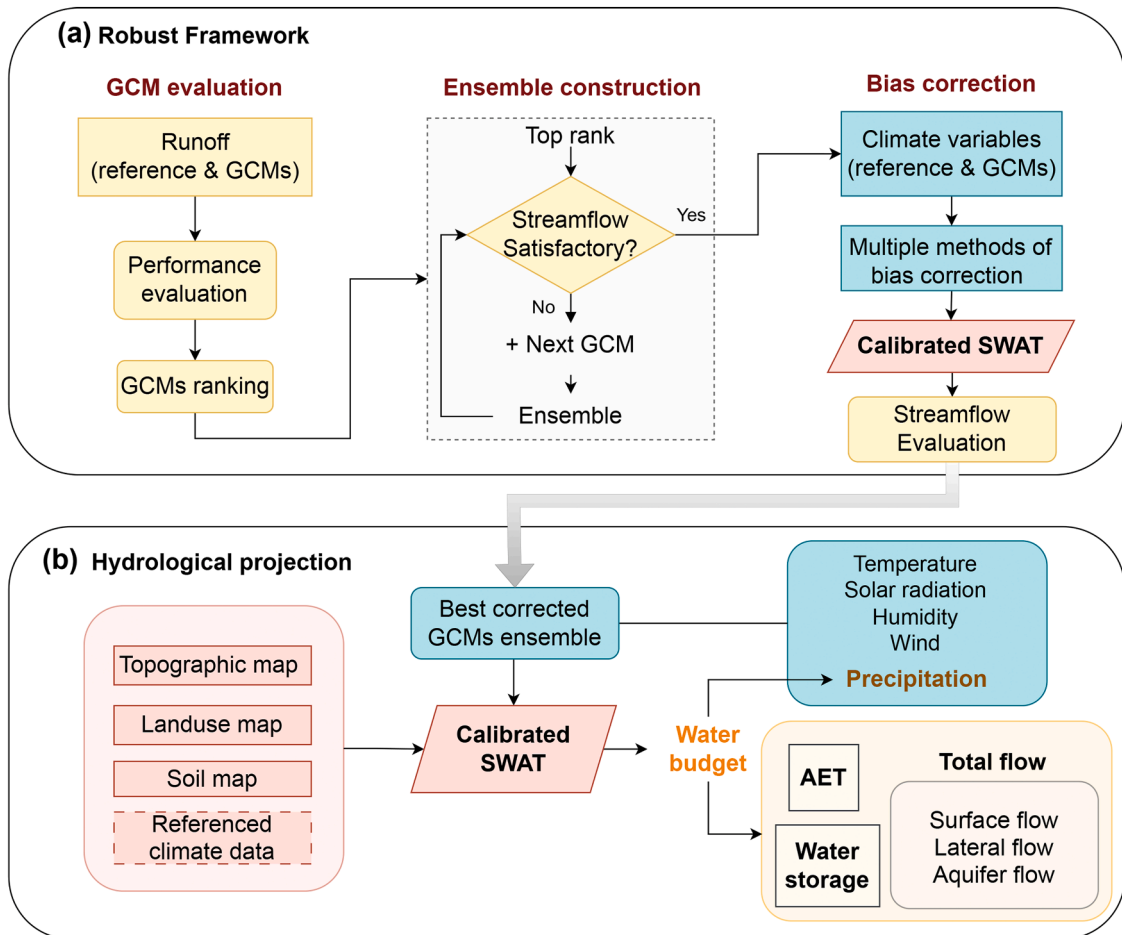


Fig. 2. Flowchart showing (a) a robust framework for constructing a subset of General Circulation Models (GCMs) and (b) Soil and Water Assessment Tool (SWAT) model for predicting water fluxes on the land surface.

mechanism of hydrological dynamics controlled by monsoon climate and land surface processes. We chose the PRB because of its typical monsoon climate, highly heterogeneous land surface, and dense population, which makes it an especially interesting case.

## 2. Dataset and method

### 2.1. Study area

The PRB in the southern China covers an area of  $4.4 \times 10^5 \text{ km}^2$  (Fig. 1). The basin has a typical subtropical monsoon climate with a total annual precipitation of 1700 mm. The distribution of precipitation exhibits spatial and temporal heterogeneity. The wet season occurs from April to September and accounts for almost 80 % of the precipitation because it receives abundant humid vapors from the East Asian Summer Monsoon (EASM) and the weakened South Asian Summer Monsoon (SASM) (Fig. 1a). In contrast, during the dry season, from October to March of the following year, the prevailing East Asian Winter Monsoon (EAWM) from the Siberian High results in little precipitation. The distribution of precipitation is affected by topography (Fig. 1b). Inland areas are more prone to showers and moderate rainfall, while coastal areas are more susceptible to heavy rainfall and affected by typhoons (Lu et al., 2021). Land use patterns are influenced by topography and local climate conditions (Fig. 1c). The Yungui Plateau in the northwest, characterized by lower precipitation and solar radiation, is predominantly covered by pasture. The northern subregions, with mountainous and hilly terrains, are dominated by forests. The central south basin, characterized by flat topography, coarse texture, abundant solar radiation and water resources, is primarily agricultural lands. The urban areas are concentrated in the Pearl River Delta (PRD) near the Pearl River Estuary.

The Pearl River has an average annual discharge of  $9631 \text{ m}^3/\text{s}$ , making it the second-largest river in China in terms of streamflow. The Pearl River has three main tributaries: the West, North, and East Rivers, which flow into three terminal gauge stations—Gaoyao, Shijiao, and Boluo, respectively (Fig. 1b). These stations are situated at the junction of rivers in the lower regions of the PRD plain and are distant from the tidal influences of the estuary. They collectively measure the total streamflow from the PRB. The basin is crucial to the approximately 124 million people living around it and contributes 15.9 % to the nation's gross domestic product. Under climate change, extreme floods and droughts extreme events are anticipated to become more frequent in the basin, thereby posing high risks to natural ecosystems and food production (Liang et al., 2019). Therefore, it is imperative to understand the mechanisms of hydrological dynamics for developing management strategies for future water resources in the PRB.

### 2.2. Multi-level calibrated framework

In this study, we developed a multi-level calibrated framework for constructing a reliable subset of GCMs (Fig. 2a). This framework incorporates hydrology to establish constraints for GCM evaluation, ensemble construction, and bias correction, rather than focusing solely on the statistical performance of climate variables as in previous studies (Guo et al., 2023; Warszawski et al., 2014). Specifically, we evaluated and ranked the GCMs based on their runoff output performance. We iteratively selected a subset of GCMs until their averaged streamflow met the satisfactory standard. We chose the bias correction method based on its capacity to improve streamflow simulation driven by the corrected climate variables. The metrics and results for each step are detailed in Sections 2.2.2 to 2.2.4.

We then utilized the bias corrected GCM subset to drive the SWAT model to simulate regional water fluxes (Fig. 2b). SWAT is a highly efficient process-based hydrological model that uses Hydrological Response Units to reflect landscape heterogeneity by integrating topography, soil properties, land use, and management practices. We used the SWAT model, which was well-calibrated and validated to simulate the spatiotemporal distribution of water fluxes in one of our previous works (Zhang et al., 2024). SWAT surpasses GCM runoff outputs by providing high-resolution insights into water budget components and reflecting hillslope hydrology and surface-groundwater interactions. The simplified water budget of SWAT is expressed as:

$$\text{Precipitation} = \text{AET} + Q_{\text{tot}} + \Delta S, \quad (1)$$

$$Q_{\text{tot}} = Q_{\text{sur}} + Q_{\text{lat}} + Q_{\text{aqu}}, \quad (2)$$

where AET represents Actual Evapotranspiration, and  $\Delta S$  represents the change in water storage;  $Q_{\text{sur}}$ ,  $Q_{\text{lat}}$ , and  $Q_{\text{aqu}}$  represent surface flow, lateral flow, and aquifer flow, respectively; and  $Q_{\text{tot}}$  represents their sum as total flow. All terms are in millimeters (mm). In our study, we use the terms 'runoff,' 'water flux,' and 'flow component' to quantify the water depth, measured in millimeters (mm) at different time scales. We use 'streamflow' specifically to describe the volumetric rate of water movement through a stream or river, measured in cubic meters per second ( $\text{m}^3/\text{s}$ ).

#### 2.2.1. Datasets

The datasets in this study included hydrology and climate components of the reference data and GCMs (Fig. 2). We evaluated the performance of the GCMs based on hindcast runoff at a monthly scale from 1995 to 2014 (20 years). Consistent with the Intergovernmental Panel on Climate Change (IPCC) report, future hydrological projections using SWAT relied on daily climate variables from 2015 to 2099 (85 years). We obtained the GCM runoff and climate data from the CMIP6 archive (<https://pcmdi.llnl.gov/CMIP6>). We selected the Shared Socioeconomic Pathway (SSP) 5–8.5 as the illustrative scenario for climate change, which is the business-as-usual pathway and stands the potential upper-bound impacts of climate change on hydrological systems. After screening to ensure the availability of historical monthly runoff and future daily climate data, we selected 33 GCMs for further analysis. Table 1 provides

details of these GCMs, including their names, spatial resolutions, and host institutions.

The reference hydrology data included the distribution of runoff generated from the validated SWAT model (Fig. S1 in Appendix A) and time series of observed streamflow at three gauge stations (i.e., Gaoyao, Shijiao, and Boluo, Fig. 1b) from the China Hydrological Yearbook. The reference climate data were AgEra5, the Global Weather for Agriculture dataset based on hourly ECMWF ERA5 data downscaled to 0.1° resolution (<https://cds.climate.copernicus.eu/cdsapp#!/dataset/sis-agrometeorological-indicators?tab=overview>). It performed much better than other datasets such as the Climate Forecast System Reanalysis, China Meteorological Assimilation Driving Datasets, and Global Precipitation Measurement (Table S1 in Appendix A). For consistency in spatial performance evaluation, the GCMs with varying spatial resolutions were linearly interpolated to the grid of the AgEra5 dataset. The climate variables from the GCMs and AgEra5 that we used to force the SWAT model included precipitation, maximum and minimum temperature, solar radiation, humidity, and wind speed.

2.2.2. GCM evaluation

We evaluated the GCMs by comparing the spatiotemporal patterns of their runoff outputs with reference datasets across three dimensions: 1) a temporal scale represented by the Nash-Sutcliffe efficiency (NSE) (Nash and Sutcliffe, 1970) of watershed streamflow, 2) a spatial scale represented by the Pearson correlation coefficient (*r*) of runoff distribution, and 3) a mean state represented by the percent bias (Pbias) of the watershed streamflow (Eqs. 3–5).

$$NSE = 1 - \frac{\sum_{i=1}^n (Y_i^{ref} - Y_i^{GCM})^2}{\sum_{i=1}^n (Y_i^{ref} - \bar{Y}^{ref})^2}, \tag{3}$$

$$r = \frac{\sum_{i=1}^n (Y_i^{ref} - \bar{Y}^{ref})(Y_i^{GCM} - \bar{Y}^{GCM})}{\sqrt{\sum_{i=1}^n (Y_i^{ref} - \bar{Y}^{ref})^2} \sqrt{\sum_{i=1}^n (Y_i^{GCM} - \bar{Y}^{GCM})^2}}, \tag{4}$$

Table 1

Overview of the Global Climate Models (GCMs) evaluated in this study, including basic information and their runoff performance.

Institution	Model	Resolution	Historical	SSP5-8.5	NSE	<i>r</i>	Pbias	Rank
AS-RCEC	TaiESM1	100 km	W	T, W	-0.76	0.71	-14.8 %	7
CAS	FGOALS-g3	250 km	W	W	-0.48	-0.44	53.84 %	23
CCCma	CanESM5	500 km	√	√	-0.68	-0.2	7.61 %	17
CMCC	CMCC-CM2-SR5	100 km	T	T	-2.44	0.34	-89.9 %	29
	CMCC-ESM2	100 km	√	√	-3.58	0.15	-65.96 %	31
CNRM-CERFACS	CNRM-CM6-1-HR	50 km	√	√	-0.88	0.52	-36.52 %	12
	CNRM-ESM2-1	250 km	√	√	-1.87	0.29	-50.18 %	19
	CNRM-CM6-1	250 km	√	√	-2.61	0.29	-62.35 %	27
CSIRO	ACCESS-ESM1-5	250 km	√	√	-3.08	0.75	-88.56 %	22
	ACCESS-CM2	250 km	√	√	-2.05	0.55	-81.55 %	20
EC-Earth-Consortium	EC-Earth3-Veg	100 km	√	√	0.16	0.53	2.47 %	1
	EC-Earth3-CC	100 km	√	√	0.37	0.52	6.39 %	2
	EC-Earth3	100 km	√	√	0.38	0.41	5.52 %	3
	EC-Earth3-Veg-LR	250 km	√	√	0.22	0.17	18.85 %	9
INM	INM-CM4-8	100 km	√	√	-4.99	0.11	-136.5 %	32
	INM-CM5-0	100 km	√	√	-5.35	0.09	-141.5 %	33
IPSL	IPSL-CM6A-LR	250 km	√	√	0.06	0.39	0.76 %	5
KIOST	KIOST-ESM	250 km	√	√	-0.36	-0.53	62.2 %	24
MIROC	MIROC6	250 km	√	√	-2.97	0.14	-52.19 %	28
	MIROC-ES2L	500 km	√	√	-2.45	-0.24	-54.77 %	30
MOHC	HadGEM3-GC31-MM	100 km	√	√	-1.62	0.78	-67.2 %	13
	UKESM1-0-LL	250 km	√	√	-0.99	0.5	-63.53 %	18
	HadGEM3-GC31-LL	250 km	√	√	-1.67	0.51	-77.25 %	21
MPI-M	MPI-ESM1-2-LR	250 km	√	√	-0.08	0.57	50.46 %	8
	MPI-ESM1-2-HR	100 km	√	√	-0.29	0.42	65.25 %	15
MRI	MRI-ESM2-0	100 km	√	√	-0.04	0.31	24.36 %	10
NCAR	CESM2	100 km	T, W	W	-0.63	0.46	-21.45 %	11
	CESM2-WACCM	100 km	T, W	T, W	-0.88	0.27	-17.57 %	14
NCC	NorESM2-MM	100 km	W	T, W	-0.23	0.68	-17.08 %	4
	NorESM2-LM	250 km	W	T, W	-0.22	0.45	-2.86 %	6
NIMS-KMA	KACE-1-0-G	250 km	W	√	-3.01	0.6	-112.7 %	24
NOAA-GFDL	GFDL-CM4	100 km	√	√	-0.1	0.06	47.31 %	15
	GFDL-ESM4	100 km	√	√	-0.41	-0.37	64.18 %	26

\*SSP represents Shared Socioeconomic Pathway. √ denotes complete variables of GCMs, and T and W indicate the absence of temperature and wind variables, respectively. All listed models include the variables of runoff, precipitation, solar radiation, and humidity. Runoff performance metrics include Nash-Sutcliffe efficiency (NSE), Pearson correlation coefficient (*r*), and percent bias (Pbias).

$$Pbias = \frac{\sum_{i=1}^n (Y_i^{ref} - Y_i^{GCM})}{\sum_{i=1}^n Y_i^{ref}} \times 100\%, \tag{5}$$

where  $Y_i^{ref}$  and  $Y_i^{GCM}$  represent the reference and GCM values, respectively, and  $\overline{Y^{ref}}$  and  $\overline{Y^{GCM}}$  represent their mean values, respectively. NSE ranges from  $-\infty$  to 1, with a value of 1 indicating perfect performance and a negative value indicating that the model performed worse than the mean value of the reference.  $r$  varies from  $-1$  to 1, with a value closer to 1 indicating better performance. The optimal value of Pbias is 0, with positive or negative values indicating that GCMs underestimated or overestimated the variable, respectively.

We initially ranked the GCMs based on these three indices: NSE,  $r$ , and Pbias. We then used a comprehensive ranking index (Eq. 6) to score each model's performance and determine its overall ranking (Tang et al., 2021):

$$score = 1 - \frac{1}{nm} \sum_{i=1}^n rank_i, \tag{6}$$

where  $m$  and  $n$  denote the number of GCMs and indices, respectively, and  $rank_i$  indicates the rank of the model for the  $i$ th index. A GCM with a score close to 1 is considered superior.

The GCMs exhibited varying levels of skill in reproducing runoff in the PRB. The metrics of NSE,  $r$ , and Pbias in individual models varied between  $-5.4$  and  $0.38$ ,  $-0.53$  and  $0.78$ , and  $-142\%$  to  $65.3\%$ , respectively (Fig. 3). The detailed metrics and ranking of each GCM are listed in Table 1.

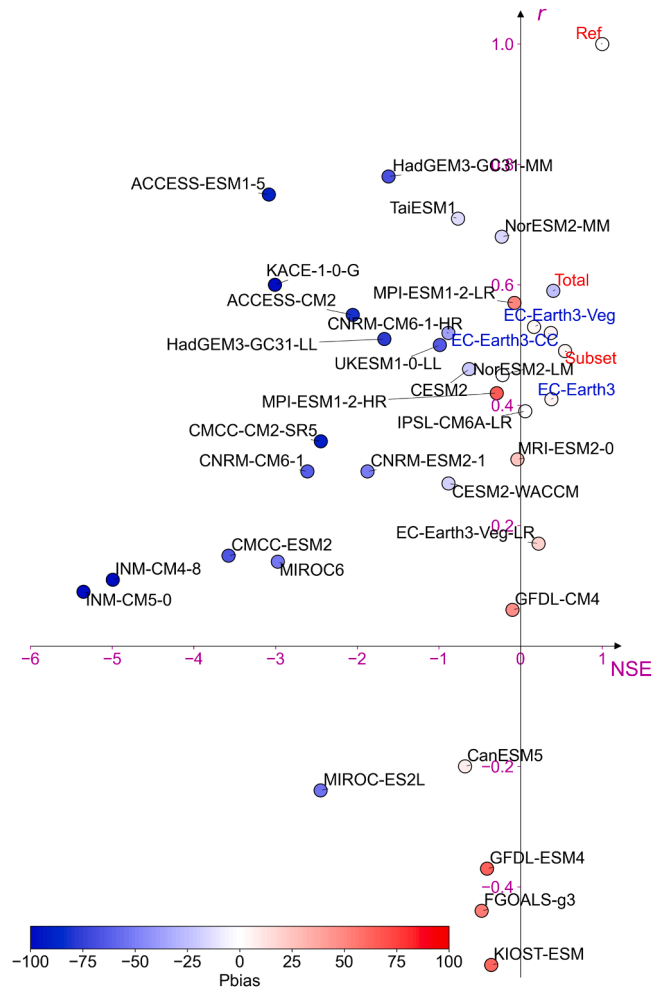


Fig. 3. Scatter plot showing the performance metrics of GCM runoff compared with the reference dataset (Ref), including Nash-Sutcliffe efficiency (NSE) on the x-axis, spatial correlation coefficient ( $r$ ) on the y-axis, and percent bias (Pbias) in color. The performance metrics of the subset and total ensemble of GCMs, and the reference dataset, are displayed in red text.

2.2.3. Ensemble construction

Selecting the GCMs involved averaging the runoff outputs of the GCMs sequentially, beginning with the highest-ranked model. This process continued iteratively, adding one model at a time until the aggregated streamflow from the selected GCMs satisfied the predetermined criteria. We introduced the widely recognized criteria in hydrological modeling research from Moriasi et al. (2007). The metrics of the criteria include the NSE, Pbias, and the Root Mean Square Error (RMSE)-to-Observations Standard Deviation (STD) Ratio (RSR), referenced in Eqs. 3, 5, and 7, respectively. We adopted the ‘satisfactory’ rating from Moriasi et al. (2007), which requires an NSE greater than 0.5, a Pbias within ± 25 %, and a RSR less than 0.7.

$$RSR = \frac{RMSE}{STD_{ref}} = \frac{\sqrt{\sum_{i=1}^n (Y_i^{ref} - Y_i^{GCM})^2}}{\sqrt{\sum_{i=1}^n (Y_i^{ref} - \bar{Y}^{ref})^2}} \quad (7)$$

In the PRB, none of the individual models met satisfactory criteria for streamflow. The total ensemble, representing the averages of the entire set of models (33 GCMs listed in Table 1), achieved NSE, *r*, and Pbias values of 0.40, 0.59, and -25.6 %, respectively. During the third iteration of the selection process, we determined a specific subset of GCM members, including EC-Earth3-Veg, EC-Earth3-CC, and EC-Earth3. The streamflow performance of this subset ensemble, with NSE, *r*, and Pbias values of 0.54, 0.49, and 4.8 %, respectively (Fig. 3), was comparable to that of the total ensemble. Moreover, both the subset and total ensembles outperformed any individual GCM. The spatial distribution of the GCM subset agreed reasonably with the reference data, with areas of high and low intensity of runoff predominantly in the east-central and southwestern parts of the basin, respectively (Fig. 4a-c). In contrast, the total ensemble had a larger area of high-intensity runoff in the northeastern region. Moreover, GCMs are limited in resolving the effects of complex terrain due to the coarse horizontal resolution of the models. The subset and total ensembles exhibited 34 % and 46 % lower distribution variations, respectively, compared to the reference data, which had a STD of 350 mm/yr. Furthermore, both ensembles showed a dry bias of -30 % in the active zones of runoff flux relative to the reference dataset, while overestimating the corresponding zone sizes.

2.2.4. Bias correction

Bias correction aims to minimize the biases in the climate variables between the GCMs subset and the reference datasets. The MBCCR package (Cannon, 2020) offers a suite of bias correction methods, including delta and linear methods, which adjust the subset ensemble by adding differences or applying ratios relative to the reference, respectively. It also provides more complex techniques such as Quantile Delta Mapping (QDM), N-dimensional probability distribution function (PDF) transform of Multivariate Bias Correction (MBCn), and Rank Resampling for Distributions and Dependencies (R2D2), which align the distribution functions of GCMs with the reference (Xue et al., 2022). The climate variables from the selected GCM subset were first bias-corrected based on the referenced climate using different methods. These corrected variables were then used to drive hydrological models to simulate streamflow. The selection of the bias correction technique was based on its capacity to improve streamflow simulation performance compared to the uncorrected subset ensemble. This enhancement was quantified using the metrics NSE, Pbias, and RSR, described in Section 2.2.3.

Different bias correction methods resulted in varying changes to the spatiotemporal patterns of climate variables and runoff (Figs. S2 and S3 in Appendix A), with a thorough evaluation metrics provided in Tables S2 and S3 in Appendix A. The statistical results of the simulated streamflow, driven by the raw subset and bias-corrected GCMs, suggested that the simple delta method is a good choice for the PRB (Table 2). Specifically, the simple delta method enhanced the NSE to range from 0.5 to 0.55, reduced RSR from 0.71 to 0.67, and decreased Pbias from 19.7 % to 10.3 %. The runoff distribution driven by the delta-corrected dataset produced runoff in the basin ranging from 500 to 1250 mm/yr, which was comparable to the reference dataset range of 500 to 1500 mm/yr (Fig. 4a and

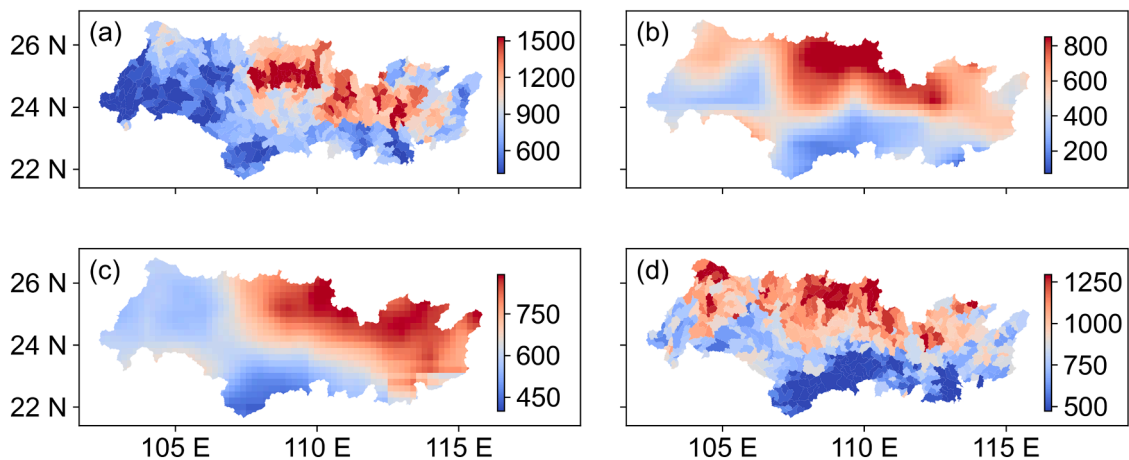


Fig. 4. Comparison of runoff distributions for (a) reference dataset, (b) subset ensemble, (c) total ensemble, and (d) SWAT results driven by the subset ensemble of GCMs after delta bias correction. All subplots are in millimeters per year (mm/yr).

**Table 2**

Statistical results of the simulated streamflow driven by the raw subset and various bias-corrected datasets.

	Mean (m <sup>3</sup> /s)	STD (m <sup>3</sup> /s)	<i>r</i>	NSE	RSR	Pbias (%)	Rank
Ref	8609	6811	1	1	0	0	
Raw	6911	4821	0.75	0.5	0.71	19.72	US
Delta	9497	5408	0.75	0.55	0.67	10.31	S
QDM	6238	5345	0.73	0.41	0.77	27.55	US
Linear	9649	1533	0.58	0.19	0.9	12.07	US
MBCn	10546	9090	0.68	-0.05	1.03	22.49	US
R2D2	9411	1490	0.03	-0.05	1.02	9.31	US

\*The bias correction methods include the delta, Quantile Delta Mapping (QDM), linear, N-dimensional probability distribution function (PDF) transform of Multivariate Bias Correction (MBCn) and Rank Resampling for Distributions and Dependences (R2D2) methods. STD refers to Standard Deviation. RSR stands for the Root Mean Square Error-to-Observations STD Ratio. The abbreviations S and US stand for the ranks of Satisfactory and Unsatisfactory, respectively.

d). Additionally, the delta-corrected dataset maintained the correct runoff distribution pattern observed in the raw subset (Fig. 4b and d). The comparison with other bias correction methods to improve streamflow performance highlights the critical importance of evaluating and selecting bias correction methods.

The seasonality of streamflow is quantified by two indices, adopted from Han et al. (2024): 1) the timing of the center of mass of streamflow (CTQ), which indicates the day of the year by which 50 % of the annual streamflow is achieved, and 2) the streamflow concentration index (QCI), which is calculated as the sum of the squares of the streamflow divided by the square of the sum, with a high value indicating a more uneven distribution of flow, typically highlighting periods of extreme flood or drought conditions.

To account for climatological conditions and to minimize the influence of interannual variability, we divided the study into four 20-year periods consistent with the IPCC reports (2021): the reference period (1995 to 2014), the near-term (2021 to 2040), the mid-term (2041 to 2060), and the long-term (2081 to 2100). We calculated the averages of the variables across these periods for our hydrological projection analysis.

### 3. Results

#### 3.1. Temporal variations of water fluxes

The delta-corrected subset of GCMs predicted temperature increases of 0.58°C in the near-term, 1.6°C in the mid-term, and 4.1°C in the long-term. Streamflow would follow a nonlinear change pattern: it would decrease insignificantly during the near-term initially and substantially increase in the long-term (Fig. 5). During the mid-term, streamflow is projected to fluctuate unstably, with a STD of 1208 m<sup>3</sup>/s, which is 1.67 times greater than the reference period and long-term. Our projected streamflow closely follows the trajectory of the raw subset ensemble ( $r = 0.9$ ), with corrections for the systematic biases between the reference and the GCM subset. Compared with the nonlinear pattern driven by the GCM subset, the total ensemble maintains a constant increase rate of 21 m<sup>3</sup>/s per year with much lower annual variations.

To understand the different stages of hydrological dynamics, we analyzed changes in water fluxes compared to the reference period (Fig. 6). Precipitation, AET, and surface flow are projected to consistently increase in the future, whereas total flow, lateral flow, aquifer flow, and water storage exhibit different trends and change patterns. During the near-term period, the increase in AET (36 mm/yr) exceeds the increase in precipitation (25 mm/yr), resulting in a 1.2 % reduction in total flow. Flow components are expected to

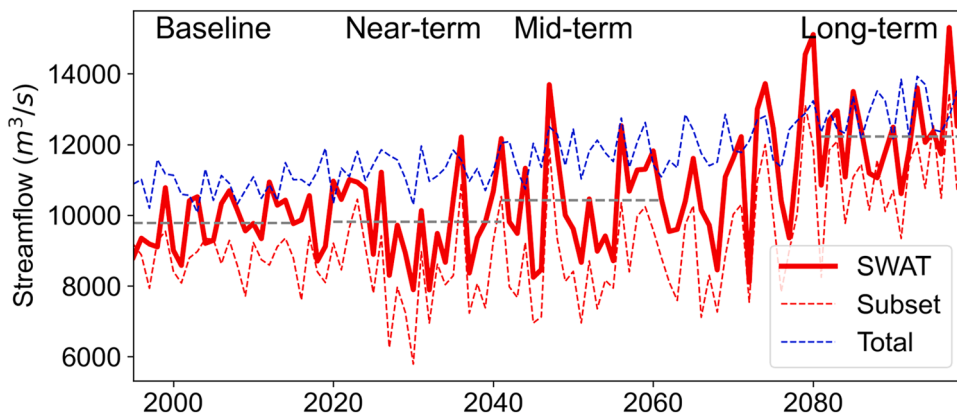


**Fig. 5.** Time series of streamflow for the entire basin from the SWAT simulation (SWAT), subset ensemble (Subset), and the total ensemble (Total) of the GCMs.

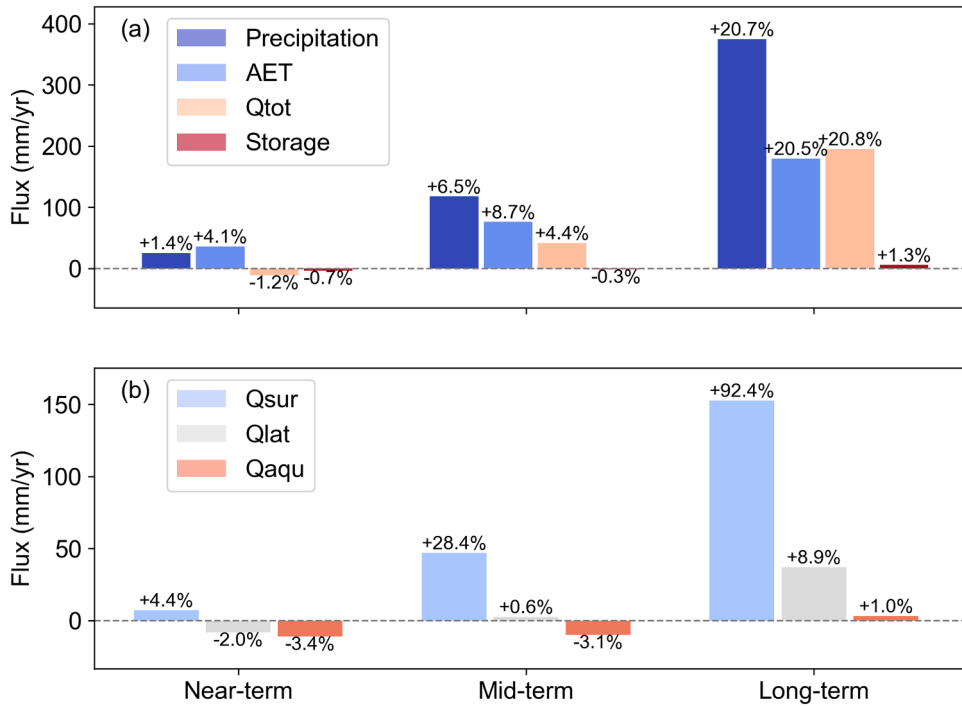


Fig. 6. Water flux changes relative to the reference period: (a) precipitation, actual evapotranspiration (AET), total flow ( $Q_{tot}$ ), and water storage; (b) surface flow ( $Q_{sur}$ ), lateral flow ( $Q_{lat}$ ), and aquifer flow ( $Q_{aqu}$ ).

respond differently: surface flow increases by 4.4 %, whereas lateral flow, aquifer flow, and water storage decrease by 2 %, 3.4 %, and 0.7 %, respectively. In the mid-term period, the increase in precipitation surpasses the increase in AET, leading to a 28.4 % rise in surface flow. Lateral flow recovers to the levels observed during the reference period, but aquifer flow and water storage remain below those levels. The most significant changes occur during the long-term period, with about a 20 % increase in precipitation, AET, and

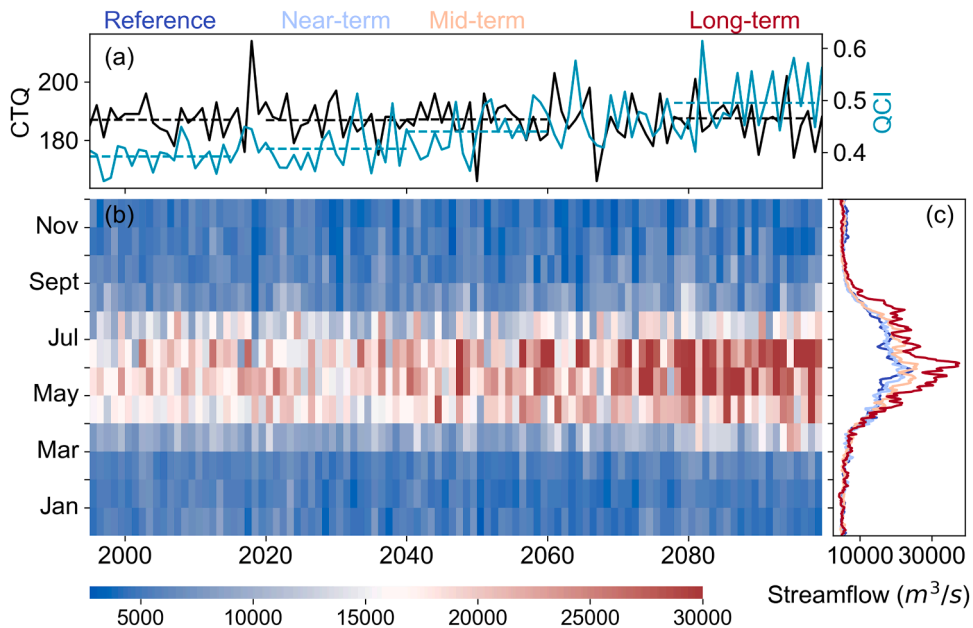


Fig. 7. (a) Time series of streamflow seasonality, including the timing of the center of mass of streamflow (CTQ) and streamflow concentration index (QCI); (b) heatmap of monthly streamflow; and (c) daily streamflow over the reference period, near-term, mid-term, and long-term periods. The dashed lines in (a) show the average values over the four periods.

streamflow. All flow components exceed the levels of the reference period, with surface flow nearly doubling by the end of the century and contributing the most to the drastic rise in total flow. However, the increases in lateral flow, aquifer flow, and water storage are more limited (< 9 %) due to constraints in subsurface storage and infiltration capacity. The consistent trend between aquifer flow and water storage indicates a strong mutual connection in their dynamics. In contrast, the differing response patterns of surface flow and baseflow highlight their varying sensitivities to climate forcing. However, as the magnitude of changes in water storage is significantly smaller compared to other hydrological variables in Eq. 1 (i.e., precipitation, AET, and total flow), this variable is excluded from further analyses.

Streamflow seasonality in the PRB is projected to intensify under the effects of climate change, as indicated by a consistent increase in the QCI, which rises from 0.4 during the reference period to 0.45 in the long term (Fig. 7a). Concurrently, the average timing of peak floods, represented by the CTQ, is likely to remain stable around the 190th day, but its annual values significantly fluctuate after the mid-term. Additionally, the streamflow trend would be distinct between the wet and dry seasons. During the wet season, streamflow is projected to increase by 38.2 % in the long term compared to the reference period (Fig. 7b and c). Notably, a substantial increase is expected in June and July, primarily driven by the summer monsoon, with a 54 % increment. Conversely, streamflow from August to October, mainly influenced by tropical cyclones, changes insignificantly, with its contribution to annual runoff increasing by less than 1 % by the century’s end. During the dry season, streamflow is projected to decrease slightly by 0.5 % at the end of the century, ultimately accounting for only 23 % of the annual streamflow.

To better understand the seasonal changes in streamflow, we compared the PDF of daily water fluxes between wet and dry seasons (Fig. 8). The total flow, precipitation, and AET during the wet season are significantly higher but less concentrated compared to the dry season. Specifically, the center values of the PDFs during the wet season are more than double those of the dry season, yet their probabilities are 50 % lower. AET throughout the year shows a clear shift towards lower probability (from 0.81 to 0.69) but higher center values (from 3 to 3.5 mm/day) from the reference period to the long term. Total flow and precipitation during the wet season exhibit a similar trend, with center values for precipitation increasing from 6.6 to 8 mm/day, and for total flow from 2.5 to 3.2 mm/day. In contrast, during the dry season, the center values for precipitation show a 12 % increase, but for total flow decrease by 10 % by the end of the century due to intensified AET.

### 3.2. Spatial variations of water fluxes

To elucidate the spatial variations in future hydrology influenced by climate change, we examined changes in total flow, precipitation, and AET across different time periods, using a reference period for comparison (Fig. 9). We found that the spatial patterns of total flow change generally align with those of precipitation (Fig. 9a-f). Notably, there is a more significant increase in total flow and precipitation in the northern and eastern parts of the basin in the near term. Over time, these zones of heightened flux shift toward the southern and eastern areas in the mid-term and long-term periods. AET is projected to increase more in higher latitude regions than in lower latitude areas (Fig. 9g-i). Although AET is increasing, its rise is less pronounced than that of precipitation, with increases peaking at 200 and 550 mm/yr, respectively, over the long-term. The consistent patterns between the runoff and precipitation, as opposed to AET, indicate that precipitation is the dominant factor influencing total flow changes (Fig. 9).

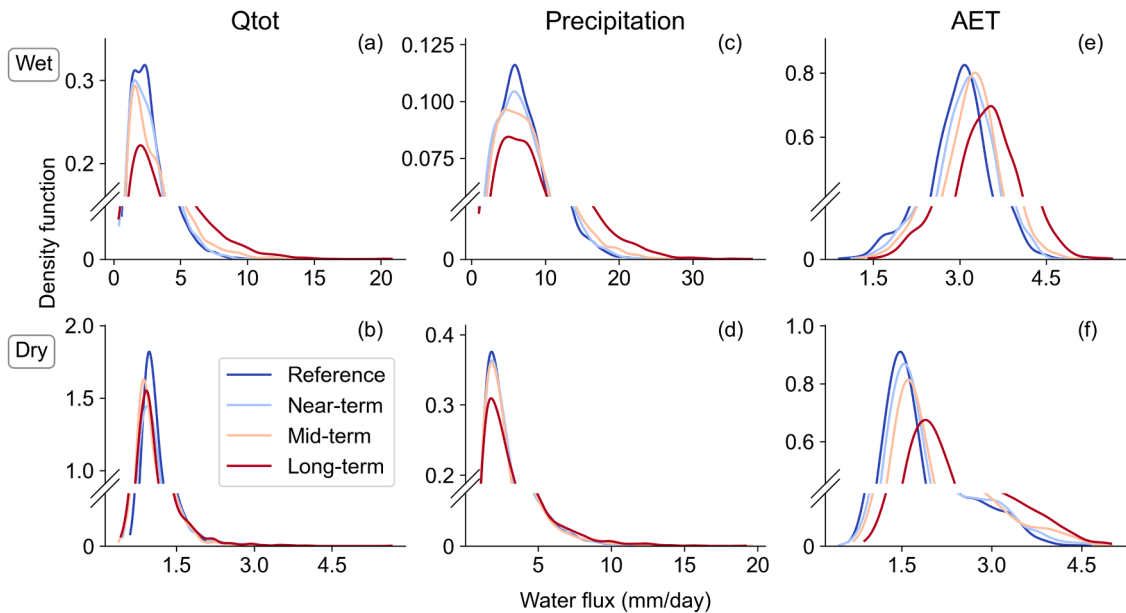
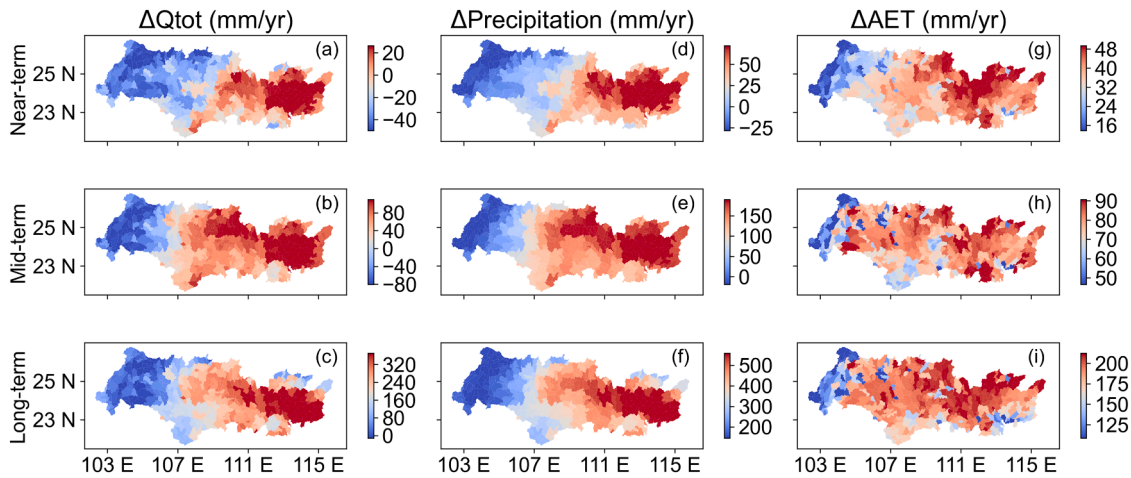


Fig. 8. Probability distributions of water fluxes during wet (upper panels) and dry seasons (lower panels). Left panels show the total flow, center panels show precipitation, and right panels show actual AET. All subplots are in millimeters per day (mm/day).



**Fig. 9.** Spatial changes in total flow (left panels), precipitation (center panels), and AET (right panels) for the future periods relative to the reference period averages. The upper, center, and lower panels represent near-term, mid-term, and long-term changes, respectively. All values are expressed in millimeters per year (mm/yr).

The changes in total flow are also zonally distinct (Fig. 9a-c). The western basin, particularly the Yungui Plateau, is projected to experience a decline in total flow during the near- and mid-term periods. In contrast, the eastern regions are expected to consistently see increases over time, with increments ranging from 20 mm/yr in the near-term to 300 mm/yr in the long-term. Overall, we expected streamflow changes to exhibit a nonlinear annual pattern, intensified seasonality, and zonal spatial disparities. These heterogeneous changes are linked to an enhanced EASM and weakened SASM, driven by differential thermal contrasts over the Pacific and Indian Oceans and the East Asian continent in response to climate change. The rationale for these spatiotemporal variations is provided in Section 4.2.

3.3. Controls on water fluxes

In addition to precipitation, we also examine the impacts of other climatic variables and land surface factors on future water fluxes. Temperature and solar radiation, for example, show patterns similar to those of AET, with a notable increase observed around the North River subbasin, which gradually extends to the northwestern basin (Figs. 10 and S4 in Appendix A). The urbanized PRD in the southeastern region is projected to experience relatively mild warming, with temperature increases of 4.6°C and solar radiation rising by 1 MJ/(m<sup>2</sup>·d) in the long term, compared to the reference period (Fig. 10a and b). In contrast, the northern high-latitude region, predominantly covered by forests, is likely to undergo significant warming, with temperature and solar radiation increases exceeding 5°C and 1.5 MJ/(m<sup>2</sup>·d), respectively.

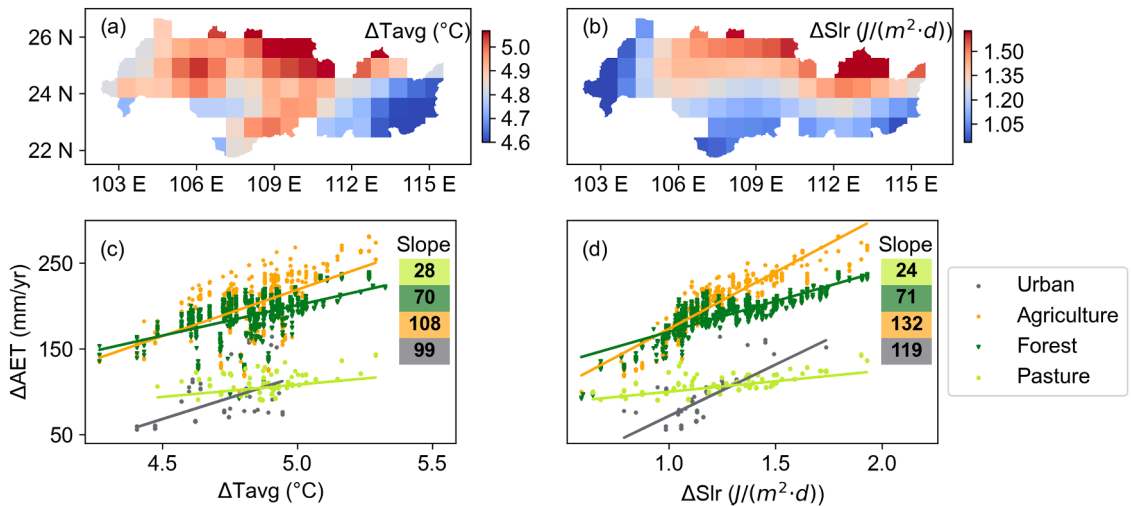


**Fig. 10.** Spatial distribution of (a) temperature and (b) solar radiation over the long term relative to the reference period averages, and the AET changes with (c) temperature and (d) solar radiation changes in various land uses.

Land use patterns reveal distinct sensitivities in the AET responses to changes in temperature and solar radiation (Fig. 10c and d). Agricultural land shows the greatest sensitivity, with annual AET increasing by 108 mm and 132 mm, respectively, for each unit increase in temperature and solar radiation, leading to a significant reduction in streamflow. In contrast, pastures display the lowest sensitivity, with annual AET increases of less than 30 mm for each factor increment. Forested land, while exhibiting a response magnitude similar to agricultural areas, demonstrates less overall sensitivity to climatic changes. Urban areas are also sensitive, but to a lesser magnitude, with AET increases only one-third of those observed in agricultural areas.

We further examined the impact of land use on flow components by analyzing their variations across different seasons and periods (Fig. 11). During the wet season, we predict a progressively significant increase in surface flow (Fig. 11a-c). This increase in urban areas is expected to be notably higher than the total flow changes in non-urban areas, rising by 50 mm/month in the long-term. In the near term, both lateral and aquifer flows are expected to decrease, subsequently recovering and surpassing levels observed in the reference period in the future. In agricultural areas, significant changes in aquifer flow are anticipated, with an increase of 6 mm/month by the long-term. Conversely, forested areas are forecasted to experience a 10 mm/month increase in lateral flow over the same period. Pastures are likely to show a similar trend to forests but with a lower magnitude of change.

During the dry season (Fig. 11d-f), the magnitude of changes in flow components is predicted to be approximately one-fifth of those observed during the wet season. Changes in surface flow are minimal during the dry season; however, there are notable decreases in lateral and aquifer flows in non-urban areas. Over the long term, agricultural areas are expected to see a decrease in aquifer flow by 8 mm/month, which could cause hydrological drought conditions for crops. In the long term, forests are expected to undergo the same overall reduction in flow (10 mm/month) as agricultural areas, but with a slightly higher reduction in lateral flow. Pastures are projected to display decreases in baseflow similar to those in forests in the mid-term, but significantly smaller than those observed in agriculture and forests, with a total reduction of 4 mm/month by the long-term. Urban areas are expected to show a decrease in surface flow during the mid-term but an increase during other periods compared to the reference period, and these changes to only 1/20th the magnitude of those observed during the wet season.

Moreover, despite similar trends of flow components between the mid-term and long-term, the change amplitudes in the long-term are approximately three times greater than those in the mid-term, for both increases during the wet season and decreases during the dry season. This suggests amplified seasonal differences in flow components over time, consistent with intensified seasonality observed in the time series of streamflow (Fig. 7). Overall, the combined variability effects of regional monsoon climate and land surface processes jointly control the spatiotemporally varied and nonlinear trend of streamflow by influencing water sources and their redistribution within the soil profile. The controlling mechanism for these factors is provided in Section 4.1.

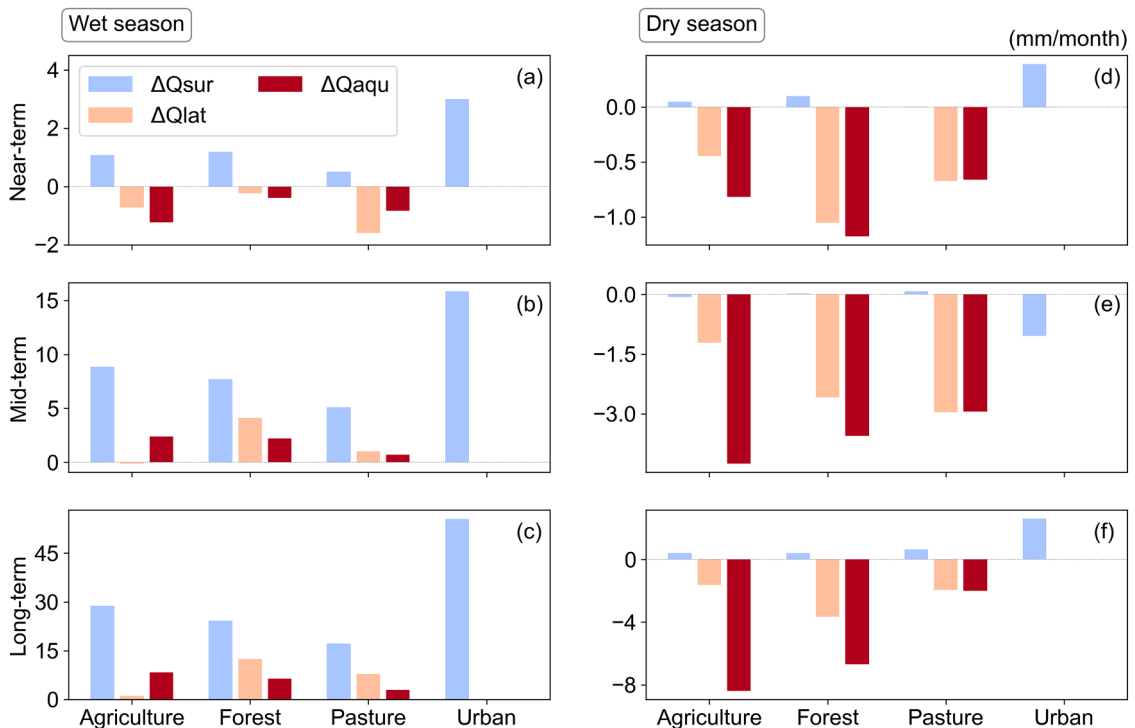


Fig. 11. Changes in flow components for future periods relative to the reference period averages during wet (left panels) and dry seasons (right panels). The upper, center, and lower panels represent near-term, mid-term, and long-term changes, respectively.

## 4. Discussion

### 4.1. Controls by monsoon climate and land surface processes

Climatic variables fundamentally govern hydrological processes in the PRB through their controls on precipitation and AET. Situated in a typical subtropical climate zone, the basin relies predominantly on precipitation as the primary contributor to streamflow. During the wet season, intensified rainfall events lead to significant increases in both streamflow and surface flow (Figs. 6 and 8). In contrast, snowfall and snowmelt processes are negligible due to the consistently high temperatures across the basin. This is in stark contrast to high-latitude permafrost regions, where snow accumulation and melt are critical components of water resources. Such regions are likely to experience more pronounced variations in baseflow under climate change because of their heightened sensitivity to snowmelt-driven hydrological processes (X. Zhang et al., 2022). In the PRB, temperature and solar radiation are the primary drivers of AET, leading to a decrease in baseflow during the dry season (Figs. 8 and 10). These bidirectional seasonal changes in streamflow partially offset each other on an annual scale, underscoring the importance of detailed studies on hydroclimate seasonality.

Different land uses, characterized by varying leaf areas, root depths, and aerodynamic roughness, impact the processes of evapotranspiration, infiltration, and water storage, thereby affecting the response of flow components to climate change (Zhang et al., 2024). The dominant flow component associated with each type of land use exhibits heightened sensitivity to climatic variations (Figs. 1c and 11) and targeted interventions are essential to mitigate the adverse hydrological consequences under climate change. Urban areas exert the most significant impact on streamflow changes due to their impermeable surfaces, which lead to consistently increasing surface flow under climate change (Fig. 11). This trend exacerbates severe flood risks, particularly when combined with intensified extreme precipitation events in the urbanized PRD. To mitigate these risks and protect human lives and infrastructure, it is imperative to enhance the integration of permeable surfaces and improve the capacity and resilience of stormwater drainage systems.

In contrast, both lateral and aquifer flows exhibit distinct seasonal trends, with increases during the wet season driven by elevated precipitation and decreases during the dry season due to heightened AET (Figs. 8 and 11). Forested areas play a crucial role in buffering hydrological extremes by creating a "sponge effect" through high interception rates (Alvarenga et al., 2016). This not only controls soil erosion during the wet season but also promotes groundwater recharge and mitigates the impacts of severe droughts during the dry season (Gomes et al., 2021). Lateral flow is particularly active and variable in the forested hills of the northern basin. Afforestation efforts in this region could further enhance this buffering capacity, reducing downstream flood risks in the PRD (Sheng et al., 2022).

Aquifer flow dominates in agricultural areas in the central-southern basin, where coarse soils with high water storage capacity prevail. However, these areas also face significant hydrological challenges under climate change. During the wet season, increased surface flow and soil erosion are anticipated, while during the dry season, intensified groundwater drought events could threaten water security, reduce agricultural productivity, and accelerate environmental degradation (Waterman et al., 2022). To address these challenges, adjustments to cropping systems are essential. For instance, flood-tolerant crops can be cultivated during the wet season, while drought-resistant crops may enhance resilience during the dry season (Yohannes et al., 2024).

The Yungui Plateau, characterized by low precipitation, is a hydrologically inactive zone within the PRB and is projected to face worsening drought conditions. However, the conversion of agricultural land to grasslands in this region offers a potential adaptation strategy. Grasslands, with their lower AET and higher infiltration rates compared to agricultural zones, could help mitigate the severity of groundwater droughts. Overall, targeted interventions for specific sub-regions are necessary to ensure sustainable water resource management and resilience to climate change in the PRB.

Furthermore, other local factors such as complex terrain, land-sea contrasts, and urban heat island effects may also influence the distribution of water fluxes. These effects are often overlooked in GCMs, which operate at coarse spatial and temporal scales (Faiz et al., 2018). Consequently, it is important to employ regional climate models such as the Weather Research and Forecasting Model, which take these effects into account, to derive more credible, finer-scale projections that accurately reflect local geographic influences on hydrological cycle (Lu et al., 2018).

### 4.2. Mechanism of spatiotemporally varied and nonlinear trend

We expected streamflow changes to exhibit a nonlinear annual pattern and zonal spatial disparities. Long-term changes are expected to be more pronounced compared to near and mid-term periods (Fig. 5), with more significant increases in the eastern parts of the basin than in the west (Fig. 9). AET is expected to rise uniformly across the region at a steady rate (2 mm/yr), driven by linear increases in solar radiation and temperature (Figs. 9 and 10). Precipitation plays a leading role in these spatiotemporal changes in streamflow and its increase during wet season gradually offsetting the increase in AET throughout the year (Figs. 8 and 9).

Precipitation in the PRB is strongly influenced by the Asian Summer Monsoon system, which transports moisture from tropical oceans to the region. This linkage is supported by evidence from stalagmite oxygen isotope records (Hu et al., 2024; Y. Wang et al., 2020). The EASM controls the movement of the summer rain belt, with embedded mesoscale convection processes bringing intense precipitation to the eastern basin (Samei et al., 1999). In contrast, water vapor transported by the SASM is prone to developing into strong convection and rainstorms when disturbed and uplifted by the mountainous terrain, resulting in precipitation in the western basin (Katzenberger and Levermann, 2024; Shi et al., 2021). Enhanced EASM and weakened SASM, driven by dynamic and thermodynamic factors, would be the key reasons behind these disparities (Wu et al., 2022; Yun et al., 2014). The dynamic component refers to changes in precipitation due to varying vertical motion, while the thermodynamic component involves changes due to varying water vapor content.

EASM precipitation is expected to increase at a faster and nonlinear rate, due to dynamic factors outpacing thermodynamic effects

as temperatures rise. Stronger EASM meridional circulation is attributed to enhanced low-level land-sea thermal contrast between the Pacific Ocean and the continent, which draws significant moisture into East Asia and thus increases precipitation (Li et al., 2019). Additionally, the westward extension of the Western Pacific Subtropical High facilitates high-level divergence and enhances low-level convergence and vorticity in the southeastern part of the PRB (Fu et al., 2016). In contrast, SASM circulation is projected to weaken almost linearly due to decreased upper-level land-sea thermal contrast between the Indian Ocean and the continent (Li et al., 2021). This weakening largely offsets the thermodynamic component's positive effects on precipitation. Consequently, precipitation in the SASM region is projected to increase quasi-linearly and slowly with climate warming, but this increase would be mainly over the ocean rather than over land, resulting in an insignificant rise in the western part of the PRB.

In contrast to the significant increase in summer precipitation, winter precipitation is projected to decrease slightly due to the weakened EAWM, contributing to intensified seasonal streamflow variations (Fig. 7). This weakening is attributed to a diminished Siberian High and a stronger eastward tilt of the East Asian Trough. These factors lead to more frequent cold surges into the North Pacific and a less disturbed winter climate in East Asia (He et al., 2014; You et al., 2022). Additionally, the diminished variability of the Aleutian Low over time may also weaken its interaction with the Siberian High, which lessens the southward movement of cold air associated with the EAWM into southern China, consequently decreasing winter precipitation (Dong et al., 2023).

Another factor contributing to the nonlinear temporal trend is aerosols, which exert significant radiative forcing through aerosol-radiation and aerosol-cloud interactions (Haywood, 2021). In the near term, precipitation increases may be initially suppressed by cooling from sulfate aerosols and atmospheric heating from absorbing aerosols. However, these mitigating effects diminish over the long term, leading to a significant rise in precipitation (Allan et al., 2020). Additionally, rapid urban development in the PRD may also have increased the frequency of rainstorms in the southeastern PRB (Wang et al., 2014).

We anticipate that the projected changes in precipitation and streamflow will extend to neighboring regions, such as the Yangtze River Basin and Southeast Asia, as these changes are driven by large-scale shifts in monsoon climate. These alterations are likely to manifest as increased intensity, frequency, and duration of summer precipitation and floods, along with heightened seasonality over the long term (You et al., 2022). These projections offer policymakers and stakeholders vital insights into future intra-seasonal and annual streamflow variations in the PRB and adjacent areas, thereby aiding in hydroclimate adaptation and water management under climate change.

#### 4.3. Reliability of hydrological projection

GCMs exhibit varying capabilities in simulating hydroclimate variables (Fig. S5 in Appendix A). It is critical to select a reliable subset of these models to ensure robust long-term projections. GCMs face challenges in providing satisfactory runoff in regional watersheds, primarily because their precipitation outputs often lag in accuracy compared to other climate variables (Fig. S5 in Appendix A). Uncertainties in precipitation are approximately an order of magnitude greater than those in other atmospheric outputs like pressure and temperature (Her et al., 2019; Willems and Vrac, 2011). In the PRB, there were substantial mismatches between the reference dataset and individual GCMs in terms of precipitation, with low spatial correlations ranging from  $-0.19$  to  $0.45$  and a mean of  $0.18$  (Fig. S6 in Appendix A). Nevertheless, the EC-Earth3 series that we selected for our study performed strongly with regards to precipitation at various temporal and spatial scales and accurately reproduced extreme precipitation events over southern China when compared to other datasets (Tang et al., 2021). Additionally, comparisons of precipitation distribution confirmed that our selected subset of GCMs aligns well with the reference dataset in identifying regions of high and low intensity (Fig. S7 in Appendix A), which further confirms the validity of our subset selection. Conversely, the total ensemble of GCMs inaccurately positioned high-intensity precipitation zones in the northeastern regions of the PRB. Moreover, the large-scale climatology of our subset ensemble closely matched the reference dataset, with similar distributions of temperature and solar radiation ( $r > 0.9$ ) and precipitation ( $r = 0.74$ ) (Fig. S8 in Appendix A). Therefore, we conclude that the subset of GCMs selected for our study effectively capture monsoon dynamics, making them well-suited for projecting runoff and precipitation in the PRB.

A reliable framework for regional hydrological projection is the prerequisite for further studies on hydroclimate vulnerability, impact, and adaptation. The multi-level calibrated framework that we propose consists of three steps: GCM evaluation, ensemble construction, and bias correction (Section 2.2). Each step aims to minimize hydrology-based uncertainty when selecting GCMs, as opposed to relying solely on climate variables and choosing the statistically optimal models. Specifically, in the GCM evaluation step, we utilized NSE,  $r$ , and Pbias as metrics to evaluate GCM runoff projections from temporal, spatial, and mean state perspectives. These metrics are straightforward, non-repetitive, and easily interpretable, providing a single index capable of measuring each dimension without compromising effectiveness (Nguyen et al., 2020). Conversely, excessive use of similar metrics can lead to redundancy and hinder the extraction of meaningful insights (Pierce et al., 2009; Zong et al., 2022). When constructing our ensemble, we avoided using the entire suite of available GCMs, arbitrary numbers of models, or recommendations from other studies. Instead, we applied robust and widely accepted criteria within the runoff modeling research: an NSE greater than  $0.5$ , a Pbias within  $\pm 25\%$ , and a RSR less than  $0.7$ . This approach strategically narrowed down the pool of GCMs, thereby reducing selection uncertainties. In the bias correction stage, we departed from the conventional practice of prioritizing the statistically 'best' climate variables in bias-corrected GCMs. Instead, we implemented various bias-corrected GCMs driving the SWAT model and selected the GCM that yielded the most accurate runoff output. The good performance of the delta method in climate variables (Tables S2 and S3 in Appendix A) also supports the effectiveness of our selection for the climatological representation.

There are many ways to improve bias correction in the future. For instance, considering the varying biases across different zones (Fig. S2 in Appendix), zoning-based approaches could be integrated into bias correction frameworks (Meema et al., 2025). Additionally, the development and combination of existing methods, such as local intensity scaling, linear scaling distribution function, and

empirical quantile mapping, warrant exploration (Ji et al., 2020; Teutschbein and Seibert, 2012). Moreover, emerging machine learning techniques—including random forests, support vector regression, long short-term memory networks, and convolutional neural networks—hold promise for enhancing the accuracy of temporal and spatial predictions (Adomako et al., 2024; Cho et al., 2020). These methods have been increasingly applied in the context of climate change, including assessments of hydrology, tropical cyclones, sea waves, and wind and solar energy (Ascenso et al., 2024; Liao et al., 2024; Sharma et al., 2024).

However, it is important to exercise caution when applying these methods. The bias in GCMs primarily stems from coarse resolution and inadequate representation of physical processes within the models (Maraun et al., 2017). Furthermore, current bias correction methods predominantly rely on statistical techniques to align model outputs with observations (Maraun, 2016). These corrections do not incorporate physical knowledge to modify the climate change signal and, therefore, cannot address the fundamental issues inherent in climate models. If misapplied, bias correction may obscure the credibility of climate projections.

Designating a perfect GCM subset is difficult due to the variation in simulation skill among many climatic variables, both temporally and spatially. Nevertheless, our multi-level calibrated framework for selecting GCMs provides reasonably accurate runoff and climate variables for the basin. Furthermore, the explicit guidelines for each step enable the potential automation of this framework, facilitating its application in climate change modeling studies worldwide.

## 5. Conclusions

This study presents a comprehensive investigation of future hydrology driven by the combined variability effects of regional monsoon climate and land surface processes. We utilized a multi-level calibrated framework for selecting a subset of GCMs and employed a well-validated SWAT model to simulate the heterogeneous water fluxes in the PRB. Based on our findings, we draw the following conclusions:

1. Streamflow in the PRB is anticipated to undergo nonlinear changes over time, characterized by a slight near-term reduction and a significant long-term increase. The streamflow shows more significant increases in the eastern parts of the basin than in the west. The spatiotemporal variations in streamflow are primarily attributed to the combined effects of enhanced/weakened EASM/SASM and land surface processes.
2. Land surface processes control the response of streamflow to climate change. Lateral flow is most variable in forested hills due to their high-water interception rates, while aquifer flow varies most in agricultural areas with their coarse soils and high-water storage capacity; Both show an increasing/decreasing trend during the wet/dry season because of elevated precipitation/evapotranspiration. Surface flow tends to have a consistent increase in urban regions due to low evapotranspiration and intensified precipitation.
3. A multi-level calibrated framework is developed for selecting GCMs subset with reduced hydrological uncertainty, which comprises GCM evaluation, ensemble construction, and bias correction. This framework is effective, reliable, and computationally efficient for driving the regional hydrological model for future projections.

## CRedit authorship contribution statement

**Gan Jianping:** Writing – review & editing, Methodology, Data curation, Conceptualization. **ZHANG YING:** Writing – review & editing, Writing – original draft, Visualization, Methodology, Investigation, Formal analysis.

## Declaration of Competing Interest

The authors declare that they have no known competing financial interests or personal relationships that could have appeared to influence the work reported in this paper.

## Acknowledgements

This work was supported by the Areas of Excellence Scheme (AoE/P-601/23-N, EARTH-HK project) and the General Research Fund (GRF 16307822,16307423) of the Hong Kong Research Grants Council. The Center for Ocean Research in Hong Kong and Macau is a joint ocean research center between the Laoshan Laboratory and the Hong Kong University of Science and Technology (HKUST).

## Appendix A. Supporting information

Supplementary data associated with this article can be found in the online version at [doi:10.1016/j.ejrh.2025.102239](https://doi.org/10.1016/j.ejrh.2025.102239).

## Data availability

I have shared the link to my data at the end of the article.

## References

- Adomako, A.B., Jamshidi, E.J., Yusup, Y., Elsebakhi, E., Jaafar, M.H., Ishak, M.I.S., Lim, H.S., Ahmad, M.I., 2024. Deep learning approaches for bias correction in WRF model outputs for enhanced solar and wind energy estimation: a case study in East and West Malaysia. *Ecol. Inform.* 84, 102898. <https://doi.org/10.1016/j.ecoinf.2024.102898>.
- Ahmadi, A., Daccache, A., Snyder, R.L., Suvočarek, K., 2022. Meteorological driving forces of reference evapotranspiration and their trends in California. *Sci. Total Environ.* 849, 157823. <https://doi.org/10.1016/j.scitotenv.2022.157823>.
- Allan, R.P., Barlow, M., Byrne, M.P., Cherchi, A., Douville, H., Fowler, H.J., Gan, T.Y., Pendergrass, A.G., Rosenfeld, D., Swann, A.L.S., Wilcox, L.J., Zolina, O., 2020. Advances in understanding large-scale responses of the water cycle to climate change. *Ann. N. Y. Acad. Sci.* 1472, 49–75. <https://doi.org/10.1111/nyas.14337>.
- Alvarenga, L.A., de Mello, C.R., Colombo, A., Cuartas, L.A., Bowling, L.C., 2016. Assessment of land cover change on the hydrology of a Brazilian headwater watershed using the distributed hydrology-soil-vegetation model. *CATENA* 143, 7–17. <https://doi.org/10.1016/j.catena.2016.04.001>.
- Asceno, G., Ficchi, A., Giuliani, M., Scoccimarro, E., Castelletti, A., 2024. Downscaling, bias correction, and spatial adjustment of extreme tropical cyclone rainfall in ERA5 using deep learning. *Weather Clim. Extrem.* 46, 100724. <https://doi.org/10.1016/j.wace.2024.100724>.
- Brands, S., 2022. A circulation-based performance atlas of the CMIP5 and 6 models for regional climate studies in the Northern Hemisphere mid-to-high latitudes. *Geosci. Model Dev.* 15, 1375–1411.
- Cannon, A.J., 2020. Reductions in daily continental-scale atmospheric circulation biases between generations of global climate models: CMIP5 to CMIP6. *Environ. Res. Lett.* 15, 064006–064006.
- Cho, D., Yoo, C., Im, J., Cha, D.-H., 2020. Comparative assessment of various machine learning-based bias correction methods for numerical weather prediction model forecasts of extreme air temperatures in urban areas. *Earth Space Sci.* 7, e2019EA000740. <https://doi.org/10.1029/2019EA000740>.
- Cook, B.I., Mankin, J.S., Marvel, K., Williams, A.P., Smerdon, J.E., Anchukaitis, K.J., 2020. Twenty-first century drought projections in the CMIP6 forcing scenarios. *Earths Future* 8, e2019EF001461. <https://doi.org/10.1029/2019EF001461>.
- Dai, A., 2021. Hydroclimatic trends during 1950–2018 over global land. *Clim. Dyn.* 56, 4027–4049. <https://doi.org/10.1007/s00382-021-05684-1>.
- Das, L., Dutta, M., Mezghani, A., Benestad, R.E., 2018. Use of observed temperature statistics in ranking CMIP5 model performance over the Western Himalayan Region of India. *Int. J. Climatol.* 38, 554–570.
- Dong, Z., Wang, L., Gui, S., Gong, H., Hu, K., 2023. Diminished impact of the East Asian winter monsoon on the Maritime Continent rainfall after the late-1990s tied to weakened Siberian High–Aleutian Low covariation. *J. Geophys. Res. Atmospheres* 128, e2022JD037336. <https://doi.org/10.1029/2022JD037336>.
- Duan, K., Sun, G., McNulty, S.G., Caldwell, P.V., Cohen, E.C., Sun, S., Aldridge, H.D., Zhou, D., Zhang, L., Zhang, Y., 2017. Future shift of the relative roles of precipitation and temperature in controlling annual runoff in the conterminous United States. *Hydrol. Earth Syst. Sci.* 21, 5517–5529. <https://doi.org/10.5194/hess-21-5517-2017>.
- Faiz, M.A., Liu, D., Fu, Q., Li, M., Baig, F., Tahir, A.A., Khan, M.I., Li, T., Cui, S., 2018. Performance evaluation of hydrological models using ensemble of general circulation models in the northeastern China. *J. Hydrol.* 565, 599–613. <https://doi.org/10.1016/j.jhydrol.2018.08.057>.
- Fan, M., Xu, J., Chen, Y., Li, W., 2021. Modeling streamflow driven by climate change in data-scarce mountainous basins. *Sci. Total Environ.* 790, 148256. <https://doi.org/10.1016/j.scitotenv.2021.148256>.
- Freedman, F.R., Pitts, K.L., Bridger, A.F.C., 2014. Evaluation of CMIP climate model hydrological output for the Mississippi River Basin using GRACE satellite observations. *J. Hydrol.* 519, 3566–3577.
- Fu, G., Liu, Z., Charles, S.P., Xu, Z., Yao, Z., 2013. A score-based method for assessing the performance of GCMs: A case study of southeastern Australia. *J. Geophys. Res. Atmospheres* 118, 4154–4167.
- Fu, S., Li, D., Sun, J., Si, D., Ling, J., Tian, F., 2016. A 31-year trend of the hourly precipitation over South China and the underlying mechanisms. *Atmos. Sci. Lett.* 17, 216–222. <https://doi.org/10.1002/asl.645>.
- Gleeson, T., Wang-Erlandsson, L., Porkka, M., Zipper, S.C., Jaramillo, F., Gerten, D., Fetzer, I., Cornell, S.E., Piemontese, L., Gordon, L.J., Rockström, J., Oki, T., Sivapalan, M., Wada, Y., Brauman, K.A., Flörke, M., Bierkens, M.F.P., Lehner, B., Keys, P., Kummu, M., Wagener, T., Dadson, S., Troy, T.J., Steffen, W., Falkenmark, M., Famiglietti, J.S., 2020. Illuminating water cycle modifications and Earth system resilience in the Anthropocene. *Water Resour. Res.* 56, e2019WR024957. <https://doi.org/10.1029/2019WR024957>.
- Gomes, L.C., Bianchi, F.J.J.A., Cardoso, I.M., Schulte, R.P.O., Fernandes, R.B.A., Fernandes-Filho, E.I., 2021. Disentangling the historic and future impacts of land use changes and climate variability on the hydrology of a mountain region in Brazil. *J. Hydrol.* 594, 125650. <https://doi.org/10.1016/j.jhydrol.2020.125650>.
- Gudmundsson, L., Leonard, M., Do, H.X., Westra, S., Seneviratne, S.I., 2019. Observed trends in global indicators of mean and extreme streamflow. *Geophys. Res. Lett.* 46, 756–766. <https://doi.org/10.1029/2018GL079725>.
- Guo, L., Shi, Y., Zhao, Y., 2023. Future projections of extreme integrated water vapor transport and population exposure over the Asian monsoon region. *Earths Future* 11, e2023EF003583. <https://doi.org/10.1029/2023EF003583>.
- Han, J., Liu, Z., Woods, R., McVicar, T.R., Yang, D., Wang, T., Hou, Y., Guo, Y., Li, C., Yang, Y., 2024. Streamflow seasonality in a snow-dwindling world. *Nature* 629, 1075–1081. <https://doi.org/10.1038/s41586-024-07299-y>.
- Haywood, J., 2021. Chapter 30 - Atmospheric aerosols and their role in climate change. In: Letcher, T.M. (Ed.), *Climate Change, Third Edition*. Elsevier, pp. 645–659.
- He, Y., Huang, J., Ji, M., 2014. Impact of land–sea thermal contrast on interdecadal variation in circulation and blocking. *Clim. Dyn.* 43, 3267–3279. <https://doi.org/10.1007/s00382-014-2103-y>.
- Her, Y., Yoo, S.-H., Cho, J., Hwang, S., Jeong, J., Seong, C., 2019. Uncertainty in hydrological analysis of climate change: multi-parameter vs. multi-GCM ensemble predictions. *Sci. Rep.* 9, 4974. <https://doi.org/10.1038/s41598-019-41334-7>.
- Holmes, K.J., Wender, B.A., Weisenmiller, R., Doughman, P., Kerxhali-Kleinfield, M., 2020. Climate assessment moves local. *Earths Future* 8, e2019EF001402.
- Hou, Y., Guo, H., Yang, Y., Liu, W., 2023. Global evaluation of runoff simulation from climate, hydrological, and land surface models. *Water Resour. Res.* 59, e2021WR031817. <https://doi.org/10.1029/2021WR031817>.
- Hu, Z., Fan, H., Liu, Y., Wu, Z., Hu, C., 2024. Separation of the Asian summer monsoon and local precipitation from stalagmite oxygen isotope records in Eastern China during the last millennium. *Quat. Sci. Rev.* 325, 108498. <https://doi.org/10.1016/j.quascirev.2023.108498>.
- IPCC, 2021. Sixth Assessment Report. URL (<https://www.ipcc.ch/assessment-report/ar6/>) (accessed 7.13.23).
- Ji, X., Li, Y., Luo, X., He, D., Guo, R., Wang, J., Bai, Y., Yue, C., Liu, C., 2020. Evaluation of bias correction methods for APHRODITE data to improve hydrologic simulation in a large Himalayan basin. *Atmos. Res.* 242, 104964. <https://doi.org/10.1016/j.atmosres.2020.104964>.
- Katzenberger, A., Levermann, A., 2024. Consistent increase in East Asian Summer Monsoon rainfall and its variability under climate change over China in CMIP6. *Earth Syst. Dyn.* 15, 1137–1151. <https://doi.org/10.5194/esd-15-1137-2024>.
- Li, J., Zhang, L., Shi, X., Chen, Y.D., 2017. Response of long-term water availability to more extreme climate in the Pearl River Basin, China. *Int. J. Climatol.* 37, 3223–3237.
- Li, Z., Sun, Y., Li, T., Ding, Y., Hu, T., 2019. Future changes in East Asian Summer Monsoon circulation and precipitation under 1.5 to 5 °C of warming. *Earths Future* 7, 1391–1406.
- Li, Z., Sun, Y., Li, T., Chen, W., Ding, Y., 2021. Projections of south Asian summer monsoon under global warming from 1.5°C to 5°C. *J. Clim.* 34, 7913–7926. <https://doi.org/10.1175/JCLI-D-20-0547.1>.
- Liang, C., Li, D., Yuan, Z., Liao, Y., Nie, X., Huang, B., Wu, X., Xie, Z., 2019. Assessing urban flood and drought risks under climate change, China. *Hydrol. Process.* 33, 1349–1361. <https://doi.org/10.1002/hyp.13405>.
- Liao, J., Li, Y., Li, J., Li, S., Peng, S., 2024. A two-module bias-correction model for sea wave hindcasting based on the long-short term memory neural network. *Ocean Eng.* 311, 118827. <https://doi.org/10.1016/j.oceaneng.2024.118827>.
- Liu, W., Zhang, B., Wei, Z., Wang, Y., Tong, L., Guo, J., Han, X., Han, C., 2024. Heterogeneity analysis of main driving factors affecting potential evapotranspiration changes across different climate regions. *Sci. Total Environ.* 912, 168991. <https://doi.org/10.1016/j.scitotenv.2023.168991>.

- Lu, W., Wang, W., Shao, Q., Yu, Z., Hao, Z., Xing, W., Yong, B., Li, J., 2018. Hydrological projections of future climate change over the source region of Yellow River and Yangtze River in the Tibetan Plateau: a comprehensive assessment by coupling RegCM4 and VIC model. *Hydrol. Process.* 32, 2096–2117. <https://doi.org/10.1002/hyp.13145>.
- Lu, X., Li, Q., Zhao, W., Xiao, A., Li, G., Yu, Z., 2021. Spatiotemporal characteristics of rainfall in South China from 1967 to 2018. *J. Appl. Meteorol. Climatol.* 60, 1333–1345. <https://doi.org/10.1175/JAMC-D-20-0191.1>.
- Lutz, A.F., ter Maat, H.W., Biemans, H., Shrestha, A.B., Wester, P., Immerzeel, W.W., 2016. Selecting representative climate models for climate change impact studies: an advanced envelope-based selection approach. *Int. J. Climatol.* 36, 3988–4005. <https://doi.org/10.1002/joc.4608>.
- Maraun, D., 2016. Bias correcting climate change simulations - a critical review. *Curr. Clim. Change Rep.* 2, 211–220. <https://doi.org/10.1007/s40641-016-0050-x>.
- Maraun, D., Shepherd, T.G., Widmann, M., Zappa, G., Walton, D., Gutiérrez, J.M., Hagemann, S., Richter, I., Soares, P.M.M., Hall, A., Mearns, L.O., 2017. Towards process-informed bias correction of climate change simulations. *Nat. Clim. Change* 7, 764–773. <https://doi.org/10.1038/nclimate3418>.
- Meema, T., Wattanasetpong, J., Wichakul, S., 2025. Integrating machine learning and zoning-based techniques for bias correction in gridded precipitation data to improve hydrological estimation in the data-scarce region. *J. Hydrol.* 646, 132356. <https://doi.org/10.1016/j.jhydrol.2024.132356>.
- Miller, O.L., Miller, M.P., Longley, P.C., Alder, J.R., Bearup, L.A., Pruiett, T., Jones, D.K., Putman, A.L., Rumsey, C.A., McKinney, T., 2021. How will baseflow respond to climate change in the Upper Colorado River Basin? *Geophys. Res. Lett.* 48, e2021GL095085. <https://doi.org/10.1029/2021GL095085>.
- Moriasi, D., Arnold, J., Van Liew, M., Bingner, R., Harmel, R.D., Veith, T., 2007. Model evaluation guidelines for systematic quantification of accuracy in watershed simulations. *Trans. ASABE* 50, 885–900. <https://doi.org/10.13031/2013.23153>.
- Nandi, S., Manne, J.R., 2020. Spatiotemporal analysis of water balance components and their projected changes in near-future under climate change over Sina Basin, India. *Water Resour. Manag.* 34, 2657–2675. <https://doi.org/10.1007/s11269-020-02551-2>.
- Nash, J.E., Sutcliffe, J.V., 1970. River flow forecasting through conceptual models part I — a discussion of principles. *J. Hydrol.* 10, 282–290. [https://doi.org/10.1016/0022-1694\(70\)90255-6](https://doi.org/10.1016/0022-1694(70)90255-6).
- Nguyen, H., Mehrotra, R., Sharma, A., 2020. Assessment of climate change impacts on reservoir storage reliability, resilience, and vulnerability using a multivariate frequency bias correction approach. *Water Resour. Res.* 56, e2019WR026022.
- Piao, S., Ciais, P., Huang, Y., Shen, Z., Peng, S., Li, J., Zhou, L., Liu, H., Ma, Y., Ding, Y., Friedlingstein, P., Liu, C., Tan, K., Yu, Y., Zhang, T., Fang, J., 2010. The impacts of climate change on water resources and agriculture in China. *Nature* 467, 43–51. <https://doi.org/10.1038/nature09364>.
- Pierce, D.W., Barnett, T.P., Santer, B.D., Gleckler, P.J., 2009. Selecting global climate models for regional climate change studies. *Proc. Natl. Acad. Sci.* 106, 8441–8446.
- Samel, A.N., Wang, W.-C., Liang, X.-Z., 1999. The monsoon rainband over China and relationships with the Eurasian circulation. *J. Clim.* 12, 115–131. [https://doi.org/10.1175/1520-0442\(1999\)012<0115:TMROCA>2.0.CO;2](https://doi.org/10.1175/1520-0442(1999)012<0115:TMROCA>2.0.CO;2).
- Sharma, S.C.M., Kumar, B., Mitra, A., Saha, S.K., 2024. Deep learning-based bias correction of ISMR simulated by GCM. *Atmos. Res.* 309, 107589. <https://doi.org/10.1016/j.atmosres.2024.107589>.
- Sheng, F., Liu, S., Zhang, T., Liu, G., Liu, Z., 2022. Quantitative assessment of the impact of precipitation and vegetation variation on flooding under discrete and continuous rainstorm conditions. *Ecol. Indic.* 144, 109477. <https://doi.org/10.1016/j.ecolind.2022.109477>.
- Shi, X., Li, K., Yang, M., Lu, X., 2021. Spatial-temporal distribution of summer extreme precipitation in South China and response of tropical ocean. *J. Geosci. Environ. Prot.* 9, 249–261. <https://doi.org/10.4236/gep.2021.93015>.
- Steffen, W., 2022. The Earth system, the great acceleration and the anthropocene. In: Williams, S.J., Taylor, R. (Eds.), *Sustainability and the New Economics: Synthesising Ecological Economics and Modern Monetary Theory*. Springer International Publishing, Cham, pp. 15–32.
- Tang, B., Hu, W., Duan, A., 2021. Assessment of extreme precipitation indices over Indochina and South China in CMIP6 models. *J. Clim.* 34, 7507–7524.
- Tang, Y., Wang, Z., 2021. Derivation of the relative contributions of the climate change and human activities to mean annual streamflow change. *J. Hydrol.* 595, 125740. <https://doi.org/10.1016/j.jhydrol.2020.125740>.
- Teutschbein, C., Seibert, J., 2012. Bias correction of regional climate model simulations for hydrological climate-change impact studies: review and evaluation of different methods. *J. Hydrol.* 456–457, 12–29. <https://doi.org/10.1016/j.jhydrol.2012.05.052>.
- Valipour, M., Batani, S.M., Gholami Sefidkoui, M.A., Raeini-Sarjaz, M., Singh, V.P., 2020. Complexity of forces driving trend of reference evapotranspiration and signals of climate change. *Atmosphere* 11, 1081. <https://doi.org/10.3390/atmos11101081>.
- Vereecken, H., Amelung, W., Bauke, S.L., Bogen, H., Brüggemann, N., Montzka, C., Vanderborght, J., Bechtold, M., Blöschl, G., Carminati, A., Javaux, M., Konings, A. G., Kusche, J., Neuweiler, I., Or, D., Steele-Dunne, S., Verhoef, A., Young, M., Zhang, Y., 2022. Soil hydrology in the Earth system. *Nat. Rev. Earth Environ.* 3, 573–587. <https://doi.org/10.1038/s43017-022-00324-6>.
- Wang, S., McVicar, T.R., Zhang, Z., Brunner, T., Strauss, P., 2020. Globally partitioning the simultaneous impacts of climate-induced and human-induced changes on catchment streamflow: a review and meta-analysis. *J. Hydrol.* 590, 125387. <https://doi.org/10.1016/j.jhydrol.2020.125387>.
- Wang, X., Liao, J., Zhang, J., Shen, C., Chen, W., Xia, B., Wang, T., 2014. A numeric study of regional climate change induced by urban expansion in the Pearl River Delta, China. *J. Appl. Meteorol. Climatol.* 53, 346–362. <https://doi.org/10.1175/JAMC-D-13-054.1>.
- Wang, Y., Hu, C., Ruan, J., Johnson, K.R., 2020. East Asian precipitation  $\delta$ 18O relationship with various monsoon indices. *J. Geophys. Res. Atmospheres* 125, e2019JD032282. <https://doi.org/10.1029/2019JD032282>.
- Warszawski, L., Frieler, K., Huber, V., Piontek, F., Serdeczny, O., Schewe, J., 2014. The inter-sectoral impact model intercomparison project (ISI-MIP): project framework. *Proc. Natl. Acad. Sci.* 111, 3228–3232.
- Wasko, C., Nathan, R., Stein, L., O’Shea, D., 2021. Evidence of shorter more extreme rainfalls and increased flood variability under climate change. *J. Hydrol.* 603, 126994. <https://doi.org/10.1016/j.jhydrol.2021.126994>.
- Waterman, B.R., Alcantar, G., Thomas, S.G., Kirk, M.F., 2022. Spatiotemporal variation in runoff and baseflow in watersheds located across a regional precipitation gradient. *J. Hydrol. Reg. Stud.* 41, 101071. <https://doi.org/10.1016/j.ejrh.2022.101071>.
- Willems, P., Vrac, M., 2011. Statistical precipitation downscaling for small-scale hydrological impact investigations of climate change. *J. Hydrol.* 402, 193–205. <https://doi.org/10.1016/j.jhydrol.2011.02.030>.
- Winter, J.M., Yeh, P.J.F., Fu, X., Eltahir, E.A.B., 2015. Uncertainty in modeled and observed climate change impacts on American Midwest hydrology. *Water Resour. Res.* 51, 3635–3646. <https://doi.org/10.1002/2014WR016056>.
- Wu, C., Huang, G., 2016. Projection of climate extremes in the Zhujiang River basin using a regional climate model. *Int. J. Climatol.* 36, 1184–1196.
- Wu, Q.-Y., Li, Q.-Q., Ding, Y.-H., Shen, X.-Y., Zhao, M.-C., Zhu, Y.-X., 2022. Asian summer monsoon responses to the change of land-sea thermodynamic contrast in a warming climate: CMIP6 projections. *Adv. Clim. Change Res.* 13, 205–217. <https://doi.org/10.1016/j.accre.2022.01.001>.
- Xue, P., Zhang, C., Wen, Z., Park, E., Jakada, H., 2022. Climate variability impacts on runoff projection under quantile mapping bias correction in the support CMIP6: an investigation in Lushi basin of China. *J. Hydrol.* 614, 128550. <https://doi.org/10.1016/j.jhydrol.2022.128550>.
- Yang, L., Feng, Q., Yin, Z., Deo, R.C., Wen, X., Si, J., Liu, W., 2020. Regional hydrology heterogeneity and the response to climate and land surface changes in arid alpine basin, northwest China. *CATENA* 187, 104345. <https://doi.org/10.1016/j.catena.2019.104345>.
- Yohannes, H., Argaw, M., Seifu, W., 2024. Impact of land use/land cover change on surface water hydrology in Akaki river catchment, Awash basin, Ethiopia. *Phys. Chem. Earth Parts ABC* 135, 103690. <https://doi.org/10.1016/j.pce.2024.103690>.
- You, Q., Jiang, Z., Yue, X., Guo, W., Liu, Y., Cao, J., Li, W., Wu, F., Cai, Z., Zhu, H., Li, T., Liu, Z., He, J., Chen, D., Pepin, N., Zhai, P., 2022. Recent frontiers of climate changes in East Asia at global warming of 1.5°C and 2°C. *Npj Clim. Atmos. Sci.* 5, 1–17. <https://doi.org/10.1038/s41612-022-00303-0>.
- Yun, K.-S., Lee, J.-Y., Ha, K.-J., 2014. Recent intensification of the South and East Asian monsoon contrast associated with an increase in the zonal tropical SST gradient. *J. Geophys. Res. Atmospheres* 119, 8104–8116. <https://doi.org/10.1002/2014JD021692>.
- Zhang, J., Gao, G., Li, Z., Fu, B., Gupta, H.V., 2020. Identification of climate variables dominating streamflow generation and quantification of streamflow decline in the Loess Plateau, China. *Sci. Total Environ.* 722, 137935. <https://doi.org/10.1016/j.scitotenv.2020.137935>.
- Zhang, J., Zhao, P., Zhang, Y., Cheng, L., Song, J., Fu, G., Wang, Y., Liu, Q., Lyu, S., Qi, S., Huang, C., Ma, M., Zhang, G., 2022. Long-term baseflow responses to projected climate change in the Weihe River Basin, Loess Plateau, China. *Remote Sens.* 14, 5097. <https://doi.org/10.3390/rs14205097>.

- Zhang, L., Dawes, W.R., Walker, G.R., 2001. Response of mean annual evapotranspiration to vegetation changes at catchment scale. *Water Resour. Res.* 37, 701–708. <https://doi.org/10.1029/2000WR900325>.
- Zhang, X., She, D., Ge, J., Cao, T., Xia, Y., 2022. Spatiotemporal variation of the water and sediment dynamics of the middle Yellow River Basin, China. *Hydrol. Process.* 36, e14783. <https://doi.org/10.1002/hyp.14783>.
- Zhang, Y., Gan, J., Yang, Q., 2024. Spatiotemporal variability of streamflow in the Pearl River Basin: controls of land surface processes and atmospheric impacts. *Hydrol. Process.* 38, e15151. <https://doi.org/10.1002/hyp.15151>.
- Zhou, S., Yu, B., Lintner, B.R., Findell, K.L., Zhang, Y., 2023. Projected increase in global runoff dominated by land surface changes. *Nat. Clim. Change* 13, 442–449. <https://doi.org/10.1038/s41558-023-01659-8>.
- Zhu, X., Ji, Z., Wen, X., Lee, S.-Y., Wei, Z., Zheng, Z., Dong, W., 2021. Historical and projected climate change over three major river basins in China from Fifth and Sixth Coupled Model Intercomparison Project models. *Int. J. Climatol.* 41, 6455–6473.
- Zong, X., Liu, X., Chen, G., Yin, Y., 2022. A deep-understanding framework and assessment indicator system for climate-resilient agriculture. *Ecol. Indic.* 136, 108597.